PHYSICAL REVIEW APPLIED **26,** 024067 (2026)

Battery-free wireless quartz-crystal-microbalance sensor operating at a range of 50 m

Motoyuki Hamana,[1] Ambuj Kumar Gautam,[1] Motoharu Haga,[2] Riki Nishihara,[1] Wenlou Yuan,[1] Fumihito Kato,[1,3] Nobutomo Nakamura,[1] Hiroki Okita,[1] and Hirotsugu Ogi[1,*]

[1]*Graduate School of Engineering, The University of Osaka, 2-1 Yamadaoka, Suita, Osaka 565-0871, Japan*
[2]*R&D Headquarters, DAICEL Corporation, Kita-ku, Osaka 530-0011, Japan and*
[3]*Department of Mechanical Engineering, Nippon Institute of Technology, Minamisaitama, Saitama 345-8501, Japan*

(Received 30 March 2026; revised 27 May 2026; accepted 28 July 2026; published 24 August 2026)

Battery-free and wireless sensing presents a crucial challenge for large-scale and inaccessible infrastructure, where the difficulty of power supply severely limits continuous monitoring. Here, we develop a quartz-crystal-microbalance (QCM) technique that enables fully passive sensing at distances exceeding 50 m, far beyond the operating range of conventional battery-free sensors. This capability is enabled by a few-millimeter-sized MEMS-QCM sensor incorporating integrated antennas for efficient coupling between mechanical resonance and free-space electromagnetic waves. On the sensor side, an extended antenna of approximately 100 mm in length is connected to the MEMS-QCM to enhance wireless signal transmission. On the instrumentation side, Yagi–Uda antennas are employed for efficient signal reception and transmission. By exploiting controlled bending of an ultrathin quartz resonator, we achieve battery-free strain sensing at distances of over 50 m. We further introduce a new sensing mechanism for displacement measurement based on polarization relaxation on the electrodeless quartz surface, which also operates wirelessly and without an onboard power source. In addition, the platform is shown to be applicable to the wireless, battery-free hydrogen-gas sensing. These results establish a general framework for long-range, battery-free mechanical and chemical sensing, opening a path toward continuous, nondestructive monitoring of social and industrial infrastructure.

DOI: 10.1103/wv9d-w2fv

I. INTRODUCTION

In recent years, the demand for remote sensing under diverse and harsh environmental conditions has increased dramatically in various fields, including biomedical diagnostics, structural health monitoring, environmental surveillance, and industrial safety. Among the multitude of sensing modalities, strain (or displacement) and gas sensors are particularly critical because of their ability to provide real-time, localized information about structural integrity [1,2], gas leakage [3,4], air quality monitoring [5,6], and physiological conditions [7,8]. These applications often involve locations that are physically inaccessible, hazardous to humans, or incompatible with frequent maintenance. Thus, the development of wireless sensors capable of reliable long-distance operation without physical wiring is of paramount importance. However, the practical deployment of such systems faces persistent challenges, especially regarding power supply and transmission range.

One of the most significant limitations of current wireless sensing systems is their dependence on embedded batteries. While batteries have enabled numerous advances in mobile and distributed sensing [9,10], they impose constraints in terms of lifetime, maintenance, and environmental sustainability. Battery replacement or recharging is often infeasible in remote, sealed, or biologically sensitive environments. Moreover, batteries increase system cost and complexity, introduce chemical hazards, and limit the sensor's operational lifespan. These constraints have motivated a growing interest in battery-free sensor technologies that can harvest energy from ambient sources, such as radio frequency (rf) signals [11], temperature gradients [12], solid-liquid contact electrification [13], or biological bodies [14–16]. Battery-free sensors enable continuous operation without the need for battery replacement, thereby reducing maintenance costs and environmental burden. These features make them particularly well suited for large-scale deployment in Internet of Things (IoT) networks and for reliable long-term use in industrial automation systems, where frequent maintenance is impractical, and system downtime must be minimized.

[*]Contact author: ogi@prec.eng.osaka-u.ac.jp

Over the past decade, significant progress has been made in the development of wireless, battery-free sensors, particularly those based on radio frequency identification (RFID). For instance, passive RFID tags have been used to detect humidity [17], pressure [18], and gases [19] by modulating the tag's impedance or resonant frequency. Similarly, surface-acoustic-wave (SAW)-based sensors have been developed for wireless interrogation, leveraging their frequency sensitivity to environmental parameters [20,21].

Despite these advances, a critical limitation remains: the effective communication range of most battery-free wireless sensors is typically confined to less than 1 m. This restriction severely hampers their applicability in large-scale infrastructures, such as bridges, pipelines, and factories, where sensors have to be deployed at extended distances from the main instrument. For example, most RFID-based sensing systems operate efficiently within 0.5 m due to power coupling limitations and signal attenuation. Even SAW-based sensors, which can offer longer read ranges than traditional RFID systems, rarely exceed the 1 m mark [22]. To date, there have been remarkably few reports of systems that can simultaneously achieve battery-free operation and wireless communication over distances exceeding 1 m while maintaining high-sensitivity sensing capabilities.

In this paper, we develop a wireless, battery-free quartz-crystal-microbalance (QCM) sensor fabricated using a novel MEMS process, achieving an operational range exceeding 50 m. This work marks a significant advance in remote sensing because QCM sensors exhibit exceptional thermal stability [23], surpassing that of conventional sensors, including SAW sensors, and thereby establishing a new standard for range, robustness, and functional versatility in passive sensing technologies. To our knowledge, there are no QCM sensors that operate at distances exceeding 1 m without wiring and batteries. By integrating the wireless, battery-free QCM technology, our system achieves real-time sensing of strain and gas concentrations without any local power source. We here demonstrate long-range, wireless, battery-free QCM sensing for strain and hydrogen-gas detection.

II. EXPERIMENTAL

A. Fabrication of QCM sensors

For developing a fully passive QCM sensor operating over long distances without batteries, we established a dedicated MEMS fabrication strategy for the mass production of high-efficiency, wireless, electrodeless QCM sensors. We principally developed two types of sensors, with lateral dimensions of 6×6 mm^2 and a thickness of 0.6 mm and 3×3 mm^2 with a thickness of 0.2 mm, respectively, as shown in Fig. 1. (In this paper, we refer to the former as a 6×6 sensor and the latter as a 3×3 sensor.)

In the 6×6 sensor, an AT-cut quartz resonator with dimensions of 1.6×1.8 mm^2 and a thickness of 13.1 μm, corresponding to the fundamental shear-vibration resonant frequency of 125 MHz, is encapsulated in glass casings: the resonator is located within the central square region and very gently supported by copper micropillars and microsupport structures protruding from the surrounding walls, without any fixed part [Fig. 1(c)]. This absence of tight mechanical contact enables oscillation with high-quality factors ($>20,000$) [24–26]. Thus, in a 6×6 sensor, the quartz crystal is mounted in an essentially unconstrained configuration. In the 3×3 sensor, the 125-MHz AT-cut quartz resonator is packaged in a slightly bent configuration as shown in Figs. 1(e) and 1(f). As will be discussed later, a quartz crystal that has undergone prebending deformation exhibits improved sensitivity to displacement.

As indicated in Fig. 1, we established MEMS-based fabrication processes to produce two types of electrodeless QCM sensor chips. Figure 8 in Appendix A schematically summarizes the fabrication procedure for the 6×6 sensors. First, a 4-inch, 300-μm-thick glass wafer was prepared with through-glass tungsten vias (150 μm in diameter), which later serve to electrically interconnect the inner and outer antennas deposited on the two surfaces [Fig. 8(a)]. In parallel, a thinner glass wafer (30 μm thick) with patterned microchannels was fabricated by wet etching. The two wafers were then bonded by thermal fusion bonding [Fig. 8(b)]. After depositing the outer antenna as an Au/Cr thin film on the bottom surface, four copper pillars (17 μm in height and 190 μm in diameter) were formed on the inner walls by electroplating. Subsequently, the inner antenna was deposited as an Au/Cr thin film [Fig. 8(c)]. Two identical bonded wafer stacks shown in Fig. 8(c) were thus fabricated. The AT-cut quartz resonators were placed inside the microchannels of one stack, where they were supported at their corners by the four copper micropillars [Fig. 8(d)]. The resonators were then sealed by laser bonding [Fig. 8(e)]. Finally, multiple identical 6×6 sensor chips were obtained by wafer dicing. Because the quartz plate and the semicircular support structure of the microchannel wall have an approximately 50 μm clearance in the in-plane direction [Fig. 1(c)], the quartz-crystal resonator is never tightly constrained, enabling it to oscillate freely. Furthermore, the distance between the internal antenna and the quartz resonator is only a few micrometers. This proximity allows even weak external electromagnetic waves to be efficiently captured internally, causing the quartz to vibrate.

Figure 9 in Appendix A illustrates the fabrication procedure for the 3×3 sensors, in which the AT-cut quartz resonators are intentionally prebent. The process involves preparation of glass wafers with through-glass copper-via interconnects, deposition of the inner and outer antennas, and formation of copper micropillars. The

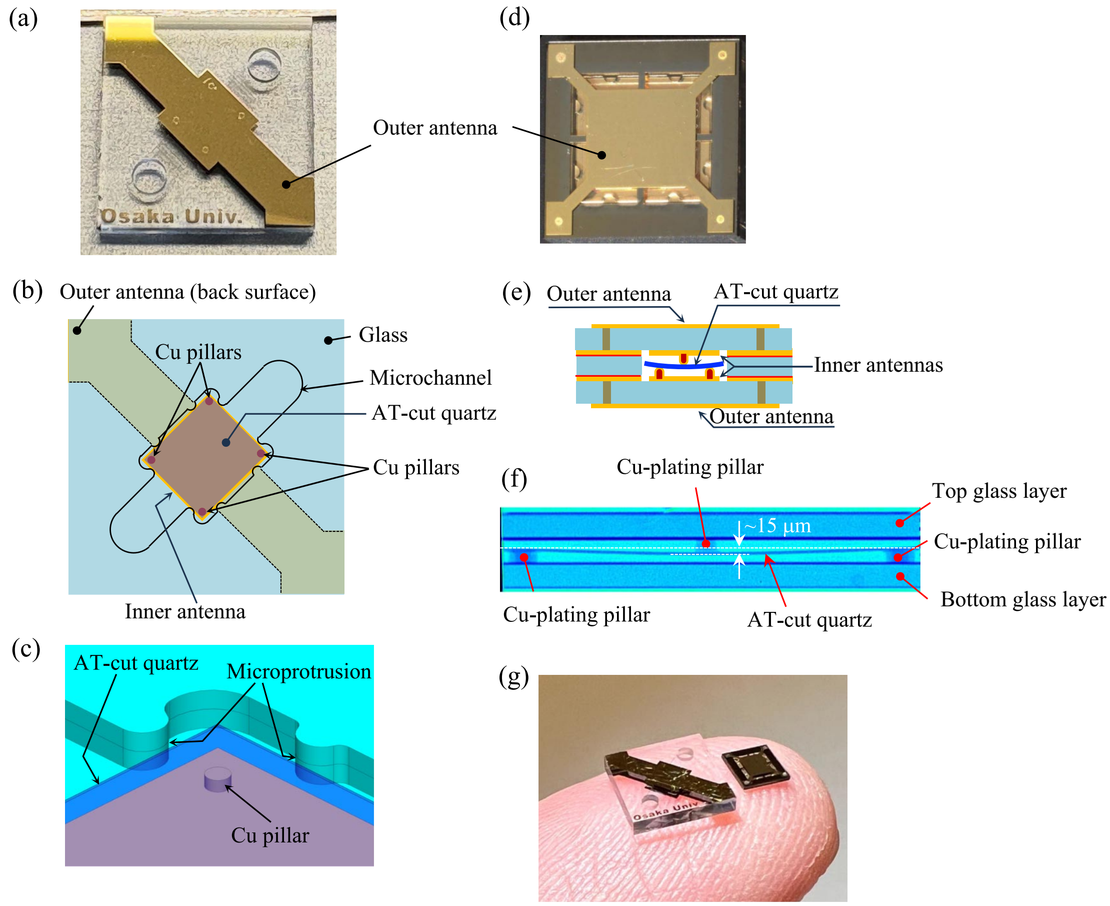

FIG. 1. Two types of MEMS-QCM sensors, featuring inner antennas. (a) Appearance of a 6 × 6 sensor, (b) its inner structure, and (c) its structure of the corner section for lightly holding the quartz resonator. (d) Appearance of a 3 × 3 sensor, (e) its cross-section structure, and (f) an x-ray-transmission cross-section image, showing that the quartz resonator is packaged in a prebent state. (g) Comparison of the appearance of the two sensors.

thickness of the intermediate glass layer was increased to 100 µm to permit larger bending of the quartz resonator. A single micropillar was formed on the upper layer to press the center of the quartz resonator and thereby create the prebent configuration [Fig. 1(f)]. The Au-Sn solder bonding was employed to package the quartz resonators. As a result, we achieved wafer-scale fabrication of 3 × 3 sensor chips incorporating prebent quartz resonators for wireless, battery-free strain sensing.

As described below, the MEMS-QCM sensor alone was insufficient to achieve long-distance wireless sensing. Therefore, an extension antenna (>approximately 100 mm in length) was connected to the integrated antenna of the MEMS-QCM sensor. Furthermore, Yagi-Uda antennas were used on the instrumentation side to enable efficient signal transmission and reception.

B. Resonant-frequency measurement

A pulser-receiver system (WRS-125) manufactured by Insight K.K. was used to excite and detect the vibration of the quartz resonator inside the MEMS sensor. Tone-burst signals with a duration of 150 µs generated by the pulser were amplified by an amplifier (ZSA5454-100K250M-O9x, Insight K.K.) to 50 V_{pp} and applied to the six-element Yagi-Uda antenna for transmission to radiate electromagnetic waves toward the sensor chip, for exciting shear vibration of the quartz resonator. The average power used for the excitation was less than 100 mW. After excitation, the resonator continued oscillating for approximately 300 µs, during which electromagnetic waves were emitted from the quartz via the antenna integrated on the sensor chip and the extension antenna. The radiated signal was received by the other Yagi-Uda antenna for detection, amplified by a 30 dB preamplifier, and digitized using a 16-bit digitizer [Fig. 2(a)]. Fourier transformation was applied to extract the amplitude and phase at the operating frequency. By sweeping the excitation frequency and recording the corresponding amplitude, the resonant spectrum was obtained. The resonant frequency was determined by fitting a Lorentzian function to the spectrum data and obtaining its center axis. We then fixed the tone-burst frequency to the measured resonant frequency and

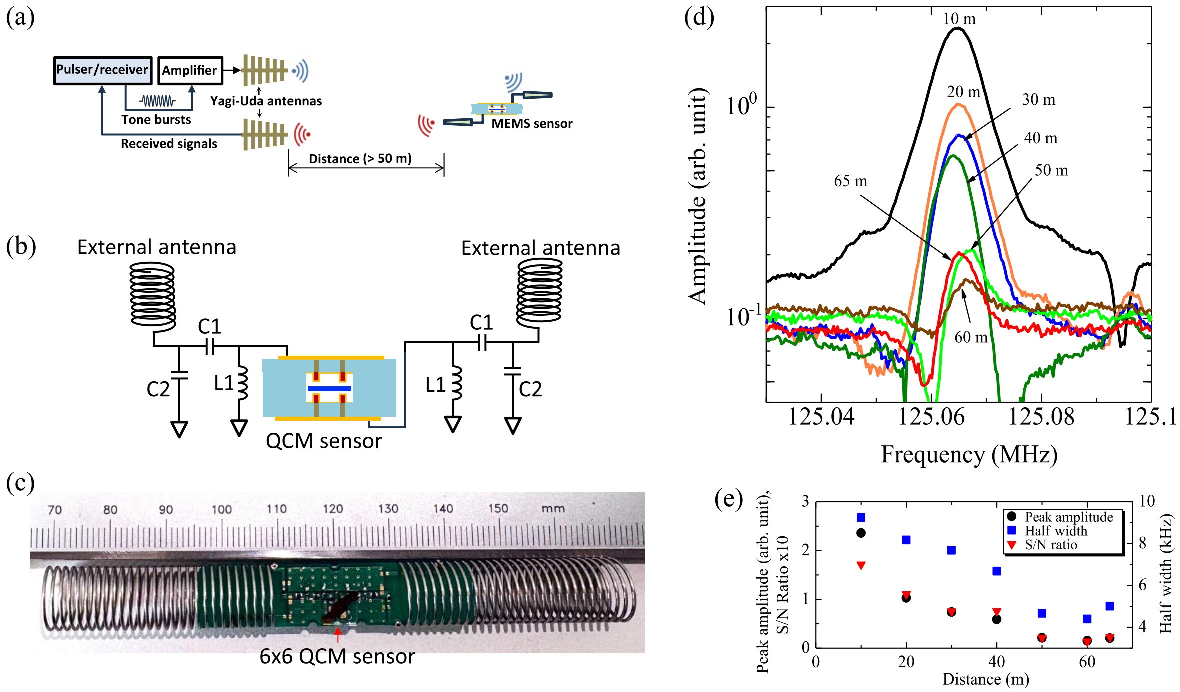

FIG. 2. Long-distance battery-free QCM experiments. (a) An illustration of the typical measurement setup. (b) The matching circuit and (c) appearance of the extended antenna. The capacitance values for C1 and C2 and the inductance value for L1 are 18 pF, 56 pF, and 100 nH, respectively. (d) Resonant spectra of the quartz resonator with distances up to 65 m from the main instrument. (e) Dependences of the resonance-peak amplitude, the signal-to-noise (S/N) ratio, and the peak half-width on the distance from the instrumentation system. The S/N ratio was calculated as the resonance-peak height divided by the baseline noise level.

monitored the change in the phase. Using a linear relationship between frequency and phase near the resonant frequency, the phase change can be converted into the frequency change [27–29].

The Yagi-Uda antenna was designed for operation at 125 MHz with a characteristic impedance of 50 Ω. It has an overall length of about 2 m along the radiation direction and lateral elements of 0.7–1 m long.

Two types of extension antennas were used. One was the compact antenna shown in Figs. 2(b) and 2(c), which was used to demonstrate the noncontact, battery-free detection of the resonant spectra of the sensor chips at 65 m distance. The other was a commercially available air-band antenna with a length of 0.36 m (NA-772, Quanzhou Truest Communication Co., Ltd.). A pair of these antennas was attached to both sides of the sensor chips for the strain measurements in Figs. 3–5 and for the hydrogen-gas experiments in Fig. 6.

The wireless experiments were conducted within an approximately 100-m-long electromagnetic shielding facility with an inner diameter of 7 m, located within the Harima Plant of Daicel Corporation (Tatsuno, Hyogo, Japan) as shown in Fig. 10 in Appendix A, so that leakage of electromagnetic waves to the outside was prevented. This was needed to ensure compliance with the Japanese Radio Law. (An application for approval is currently under review by the Ministry of Internal Affairs and Communications in Japan.)

III. RESULTS AND DISCUSSION

We first demonstrate the long-range, battery-free operation of the sensors that can be achieved by using Yagi-Uda antennas tuned at the operating frequency and by attaching extended antennas to the outer antennas [Fig. 2(a)]. As shown in Figs. 2(b) and 2(c), the antenna extension is implemented by coupling two solenoid-coil antennas to both surfaces via a battery-free matching circuit. Using the measurement system described in the experimental section, we measured the resonance spectra of a 6×6 sensor while progressively increasing the distance between the driving instrument and the sensor. The results are presented in Fig. 2(d). Although the resonant-peak amplitude and the S/N ratio decrease with increasing distance as shown in Fig. 2(e), a clear resonance peak remains observable even at a separation of 65 m from the measurement instrument. The half-width also decreases with the distance, but this may be caused by the distortion of the resonance-peak shape due to a lower S/N ratio, reducing the reliability of the calculated half-width. (It is unlikely that the half-width has actually decreased.) We thus find that this system establishes a previously unachieved capability for battery-free QCM experiments operating over distances of 50 m. This has been made possible by the internal antennas formed on the inner walls inside the sensors that provide electromagnetic fields of sufficient strength to efficiently drive the quartz resonator. Although an extension antenna incorporating a matching circuit is used, the overall sensor length of approximately 100 mm remains acceptable for infrastructure health monitoring applications.

Because the frequency bandwidth allocated by the Ministry of Internal Affairs and Communications, Japan, is typically extremely narrow, measurements must be performed within a limited frequency range, and it is essential to ensure that only a single frequency is observed within such a narrow range. As shown in Fig. 2(d), these requirements are confirmed to be satisfied.

Next, we propose long-range, battery-free displacement sensing using a 6×6 sensor, where a through-hole is machined in the top glass layer, and a contact probe is inserted to induce controlled bending deformation of the quartz resonator [Fig. 3(a)]. It has been shown that the resonant frequency of an AT-cut quartz resonator varies depending on its bending curvature [25,30]. Owing to the extremely small thickness of the resonator, it can undergo large, flexible bending deformations, as shown in Movie S1 in Supplemental Material [31]. The fracture stress of quartz is approximately 150 MPa [32], and an FEM calculation predicts that the maximum bending stress at the center of the resonator induced by a central deformation of several tens of micrometers will be well below the fracture strength [Fig. 3(b)], thereby producing a substantial frequency shift without inducing failure. We applied the deformation by actuating the contact probe from the top using a fine-pitch micrometer screw. Figure 3(c) shows the relationship between the bending deformation and the shift in resonant frequency for measurement distances of 0 m (wired configuration) and 50 m.

First, it is noteworthy that even at a long distance of 50 m, the frequency response and measurement accuracy

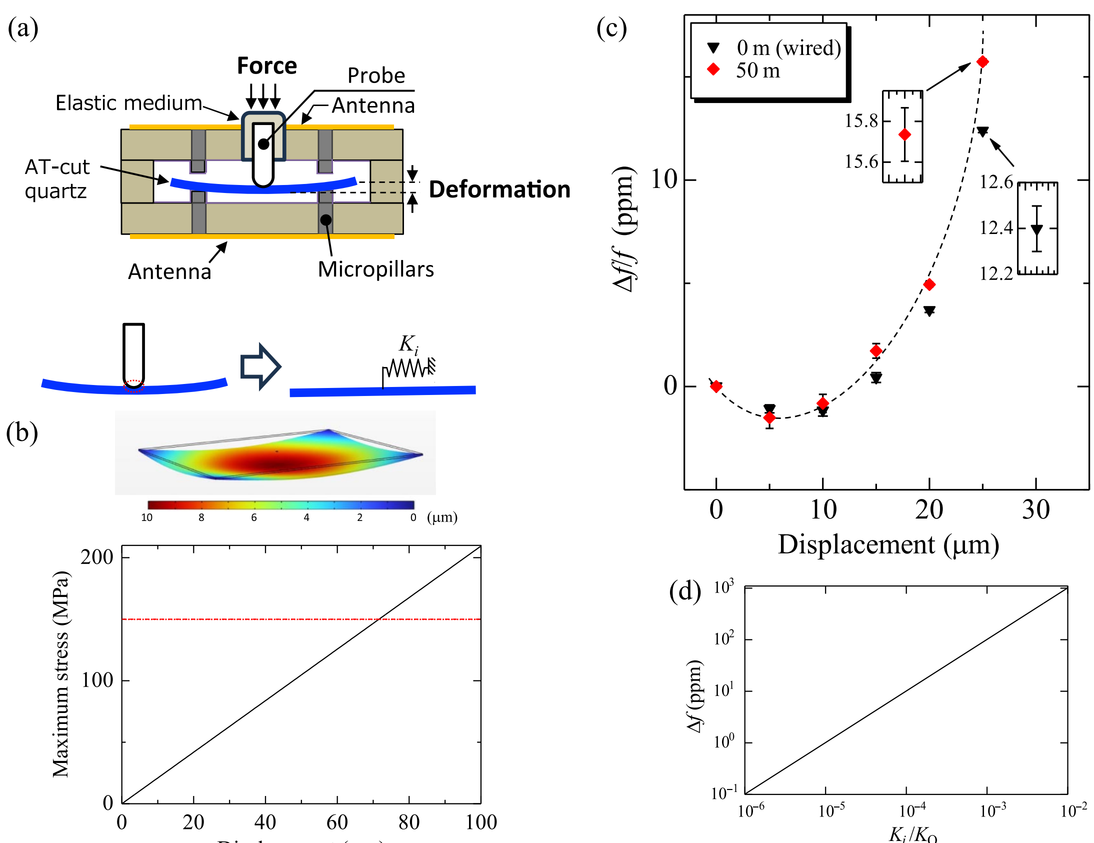

FIG. 3. Displacement sensing using bending deformation of quartz resonator. (a) Bending deformation of the quartz resonator induced by a contact probe (upper) and a spring-based model of the contact interface representing the in-plane contact stiffness K_i (lower). (b) (Upper) Finite-element-method (FEM) calculation of deformation of a 13.1-μm-thick AT-cut quartz plate with 1.8×1.6 mm^2 area supported at the four corners caused by a normal force of 1.2 mN applied on the center area. (Lower) Relationship between the maximum bending stress and the center deformation obtained by changing the applied force. The red broken line indicates the fracture stress. (c) The resonant-frequency shift caused by the deformation of the quartz resonator measured at 0 m (or wired) and at 50 m. (d) Relationship between the resonant frequency and the contact-stiffness ratio, K_i/K_Q, where K_Q denotes the equivalent spring constant of the quartz resonator.

equivalent to the wired measurement have been achieved, demonstrating excellent performance as a battery-free displacement sensor for long-distance applications. The resonant frequency decreases at small deformation but increases as the deformation becomes larger. Previous studies indicate that the resonant frequency decreases as bending deformation progresses because of the curvature [30], which explains the initial frequency decrease. However, the subsequent significant increase in frequency cannot be explained solely by the change in geometry, and we further propose an alternative mechanism that incorporates the concept of interfacial contact stiffness. Because the probe-quartz contact constrains the in-plane motion of the quartz resonator, it increases the apparent shear modulus of the resonator, leading to an increase in the resonant frequency. This interface can be modeled as an effective elastic spring, as depicted in the lower figure of Fig. 3(a), with a spring constant, K_i, that is expected to increase with the applied normal force, in analogy with Hertzian contact mechanics [33–35]. As shown by the analysis in Appendix B, an increase in the contact stiffness leads to an upward shift of the resonant frequency [Fig. 3(d)]. Applying the principle discovered here, we have developed a wireless strain sensor that operates over long distances without batteries.

Here, a crucial finding in Fig. 3(c) is that inducing a prebending deformation of approximately 15 μm significantly improves the sensitivity to displacement. Therefore, the 3×3 sensor was fabricated in which the quartz resonator was intentionally prebent by supporting its four corners from below with four micropillars while pressing the central region from above with a single micropillar. The detailed fabrication procedure is provided in Fig. 9 in Appendix A. Figure 1(f) presents an x-ray transmission cross-section image of a fabricated sensor chip, confirming that the quartz-crystal resonator is encapsulated in a prebent, deformed configuration.

Figure 4 demonstrates the outstanding long-range (50 m) strain-sensing performance of the 3×3 sensor. An acrylic cantilever beam was clamped at one end, and a 3×3 sensor was mounted on its upper surface near the fixed end. Controlled bending was applied by a microstage at the free end [Fig. 4(a)]. The resulting deformation of the beam is transferred to the sensor, which in turn modulates the curvature of the prebent quartz resonator embedded within it, leading to a measurable shift in the resonant frequency (Fig. 11 in Appendix A). The strain caused by the deformation was evaluated by a conventional strain-gauge method as shown in Fig. 4(b). The experiments were conducted under both tensile and compressive bending

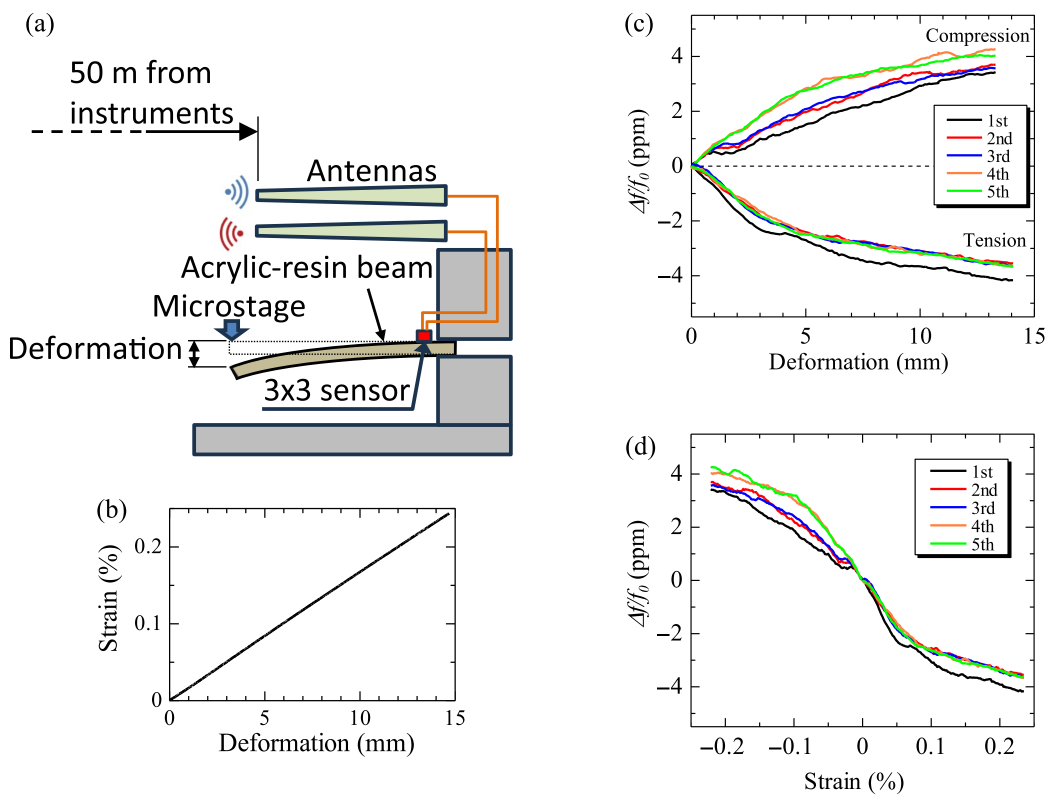

FIG. 4. Wireless, battery-free strain measurement at a distance of 50 m. (a) Schematic illustration of the experimental setup for applying the tensile strain to the sensor. The cantilever was inverted for the compressive strain. (b) Relationship between the free-end deformation and the strain measured by a strain gauge. (c) Relationship between the resonant-frequency shift and the free-end deformation and (d) that between the resonant-frequency shift and the surface strain measured at a distance of 50 m.

conditions by inverting the cantilever specimen. As shown in Fig. 4(c), the amount of the frequency shift increases with the progress of the deformation, confirming that the device sensitively detects the bending strain. Figure 4(d) shows the relationship between the strain and the frequency shift obtained for five experiments. Linearity deteriorates under larger deformations, indicating a nonlinear relationship between bending deformation and the resulting frequency shift. Although the reproducibility remains limited, to the best of our knowledge, no prior studies have achieved a strain measurement at distances over 50 m without the use of batteries, underscoring the significance and unprecedented nature of the performance of the developed sensor.

We further propose an alternative deformation-sensing mechanism based on polarization relaxation in an electrodeless quartz resonator. In piezoelectric materials, the electromechanical coupling associated with the piezoelectric effect increases the apparent elastic stiffness, thereby elevating the mechanical resonance frequencies, known as the piezoelectric-stiffening effect [36]. When surface electrodes are present, they partially weaken surface polarization, leading to a reduction in the resonance frequency. Significantly, such polarization relaxation is not limited to directly deposited electrodes: metallic objects and even dielectric materials placed in close proximity can induce a similar effect through the flow of induced charges in conductors and the polarization of nearby dielectrics in response to the surface electric field. Figure 5 validates this principle. An edge of the blank AT-cut quartz resonator was fixed to a plastic base, and flat antennas were positioned on both sides with 0.5 mm distances. A 0.1-mm-thick aluminum sheet (8×5 mm^2) was then inserted by a microstage between the resonator and one of the antennas, as illustrated in Fig. 5(a), and the resonance frequency was measured at a distance of 50 m without the use of batteries. As the overlapping area between the quartz and the aluminum sheet increased, the resonant frequency of the quartz resonator decreased markedly [Fig. 5(b)]: when the aluminum sheet fully covers the quartz resonator, a frequency shift more than 40 ppm is observed, which is approximately an order of magnitude greater than the maximum shift recorded under strain, as shown in Fig. 4, demonstrating that this mechanism enables battery-free long-range displacement sensing.

Our finding that the QCM sensor developed here can operate as a purely passive device over distances of tens of meters, without any onboard power supply, has far-reaching implications. First, it opens new avenues for deploying high-resolution chemical and mechanical sensors in locations previously deemed inaccessible without external power. This is particularly relevant to structural monitoring of civil infrastructures and to industrial safety in environments where human access is difficult. For example, as demonstrated in Fig. 6, this approach readily enables

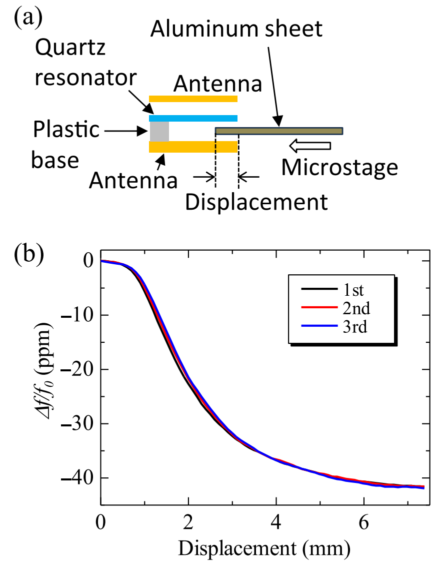

FIG. 5. Displacement sensing based on piezoelectricity relaxation phenomenon at a distance of 50 m. (a) Schematic of the experimental setup. The blank AT-cut quartz resonator ($1.8 \times 1.6 \times 0.0131$ mm^3) was fixed to the plastic base at its edge using adhesive, and the 0.1-mm-thick aluminum sheet was inserted so that its area overlapped with the quartz plate. (b) Resonant-frequency change with increasing the insertion distance of the aluminum sheet measured at a distance of 50 m in a battery-free manner.

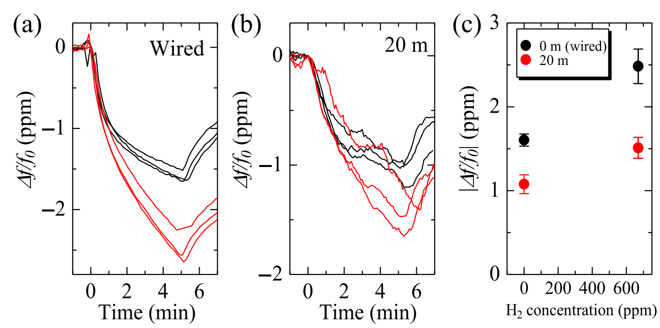

FIG. 6. Hydrogen-gas detection through Pd-alloy thin film. A 200-nm-thick Pd thin film was deposited on a single side of the quartz resonator using a magnetron-sputtering method, and H_2 gas was detected through the bending deformation of the quartz resonator caused by the volume expansion of the Pd film when it absorbed hydrogen molecules [30]. The flow injection system was used to inject 670-ppm H_2 gas during the carrier flow of a high-purity N_2 gas. A 6×6 sensor was used for these experiments. In (a) and (b), the carrier gas was switched to the sample gas at 0 min and returned to the carrier gas. Red lines represent the frequency changes when a 670-ppm H_2 gas was injected, while black lines are those when a N_2 gas (or 0 ppm H_2 gas) was injected. (a) Wired measurements and (b) battery-free measurements at a distance of 20 m. (c) Comparison of the magnitude of the frequency change caused by the gas injection between the wired and the long-range experiments.

remote, battery-free hydrogen-gas sensing, providing a powerful platform for the continuous monitoring of hydrogen-gas concentration in nuclear power facilities. Second, it establishes a scalable framework for constructing distributed networks of passive sensors, eliminating the complexity, cost, and reliability issues associated with batteries and periodic maintenance. Third, the long-range, maintenance-free operation of this platform is expected to substantially reduce system-level costs and to accelerate adoption across both emerging and mature technological sectors.

Figure 7 illustrates representative applications enabled by this sensing platform that were previously unattainable. Conventional infrastructure inspection relies primarily on periodic, discrete measurements; by contrast, our sensors support quasi-permanent data acquisition, allowing a transition to maintenance strategies based on continuous monitoring. Moreover, when coupled with artificial intelligence, the persistently available sensor signals can be exploited not only to extract target information but also to infer latent system-level information, including early signs of equipment malfunction in industrial facilities and patterns of human activity within the monitored environment.

Currently, the overall system developed here is summarized as follows. On the sensor side, a few-millimeter-scale MEMS-QCM sensor, together with an extension antenna approximately 100 mm or longer connected to it, is required. On the instrumentation side, the system consists of a pulser-receiver for transmitting and receiving burst waves, an amplifier for signal amplification, and a pair of Yagi-Uda antennas that provide highly directional transmission of the amplified signal toward the sensor as well as efficient reception. In general, the relatively large size of the instrumentation side is not a critical limitation for social infrastructure health monitoring applications. Measurements can be performed from a fixed base station,

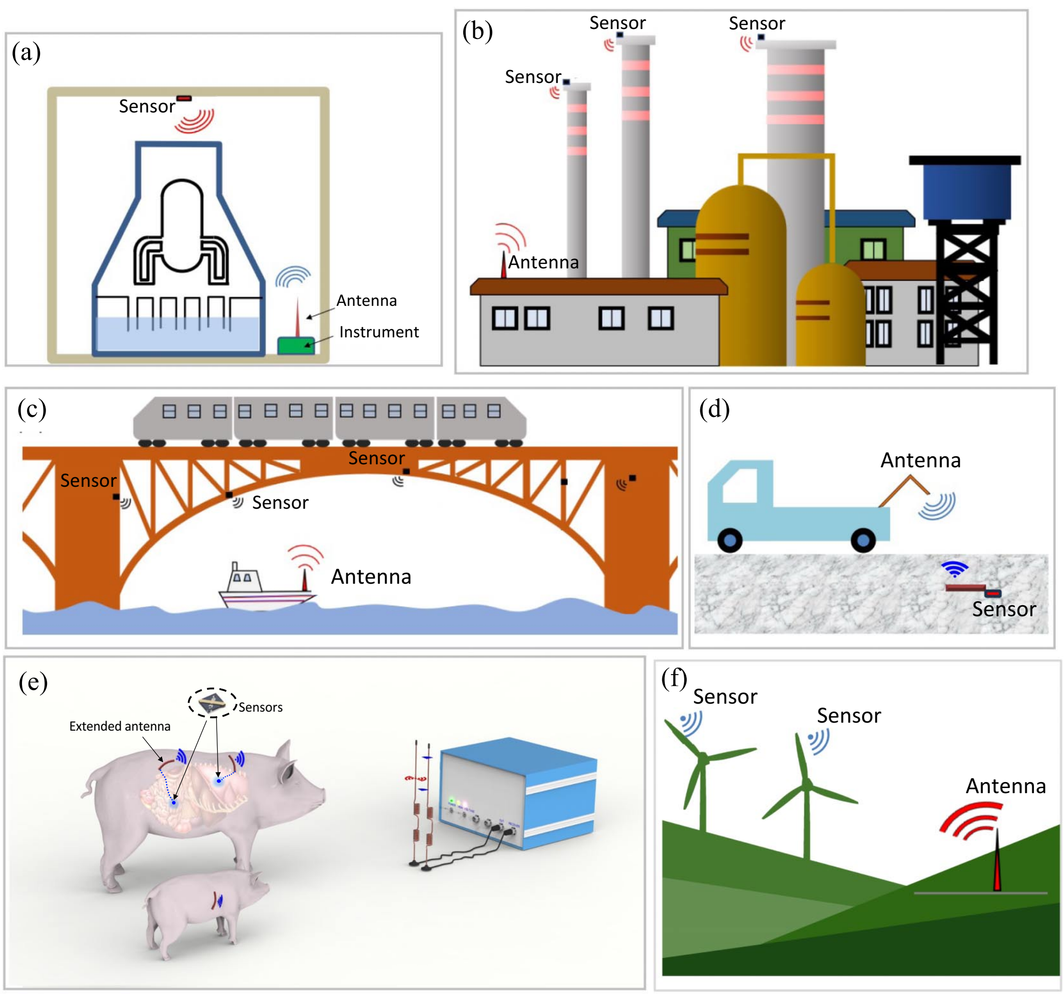

FIG. 7. Possible applications of the wireless, battery-free QCM system developed here. (a) Semipermanent measurement of hydrogen-gas concentrations in nuclear power plants. (b) Continuous monitoring of hazardous gases at very high chimney outlets. (c) Continuous monitoring of deformation and stress in bridges. (d) Monitoring the integrity of concrete structures. (e) Long-term monitoring of internal signals in animals. (f) Monitoring the integrity of rotating wind turbines.

and by miniaturizing the Yagi antenna to a three-element configuration, the system can be mounted on vehicles or helicopters. In contrast, on the sensor side, when the sensor is implanted in an animal as shown in Fig. 7(e), the extension antenna should be placed either outside the body or directly beneath the skin.

Finally, we discuss baseline stability. In QCM systems, the baseline is inherently stable due to the excellent temperature stability of AT-cut quartz crystals. For example, as shown in Fig. 11 in Appendix A, even during continuous measurements over approximately 1 h, the baseline variation remains within ± 1 ppm. However, in practical field applications, the sensor response may be influenced by various factors, including significant temperature and humidity fluctuations in the measurement environment, obstruction of the propagation path between the antenna and the sensor, and interference from other radio frequency devices. Nevertheless, since the proposed measurement system enables continuous monitoring of the sensor response, it is possible to perform analyses that account for such baseline variations. In particular, when detecting dynamic resonances in structures such as bridges, the relative frequency variation is of primary importance (i.e., the structural resonance frequency), and baseline drift induced by environmental changes is expected to have only a limited impact.

IV. CONCLUSIONS

We have established a new paradigm for long-range, battery-free sensing based on QCM technology. We have developed fully passive sensor chips and a wireless measurement system that require no onboard power supply and enable quantitative QCM measurements over distances exceeding 50 m. Beyond wireless operation, we introduced a displacement-sensing scheme based on the direct bending of quartz resonators, revealing that prebent crystals exhibit markedly enhanced displacement sensitivity. This insight led to the realization of a MEMS-packaged QCM sensor in which the resonator is intentionally precurved, providing a robust and highly responsive platform for mechanical sensing. Using this device, we demonstrated remote strain measurements over a 50 m separation, establishing the feasibility of long-distance, battery-free mechanical monitoring. Furthermore, we uncovered and exploited a dielectric relaxation mechanism unique to bare quartz resonators, enabling a distinct mode of displacement sensing that also operates at a range of 50 m. In addition to mechanical sensing, we showed that the same platform can function as a remote, battery-free hydrogen-gas sensor, highlighting the versatility of the proposed architecture.

These advances position passive QCM-based sensors as a powerful foundation for distributed, maintenance-free sensing networks. Although challenges remain for practical implementation, including further miniaturization of the extension antenna attached to the sensors and overall downsizing of the data-acquisition system, we anticipate that such sensors will play a pivotal role in safeguarding the integrity of critical social and industrial infrastructure, enabling continuous, high-fidelity monitoring in environments where conventional powered sensors are impractical or impossible.

ACKNOWLEDGMENTS

This work was supported by JSPS KAKENHI under (Grant No. 24K21578).

DATA AVAILABILITY

The data that support the findings of this study are available from the corresponding author upon reasonable request.

APPENDIX A: FABRICATION PROCESSES FOR WIRELESS-QCM SENSOR CHIPS

MEMS processes for fabricating 6×6 sensors and 3×3 sensors are shown in Figs. 8 and 9, respectively.

Figure 10 shows the 100-m-long tunnel facility where all experiments were conducted.

Figure 11 shows the frequency changes by applying the cyclic tensile and compressive stresses.

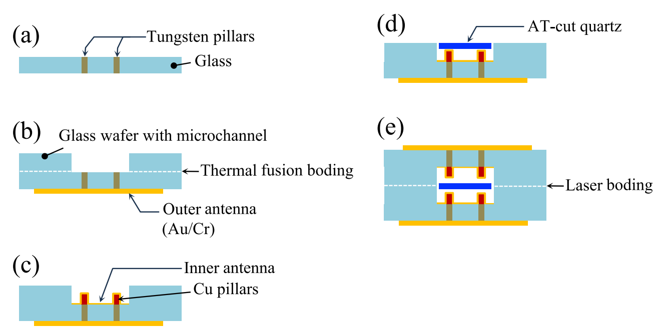

FIG. 8. MEMS processes for fabricating 6×6 sensors. (a) Preparation of 4-inch, 300-μm-thick glass wafers with through-glass tungsten vias with a diameter of 150 μm. (b) Bonding of the 30-μm-thick glass wafer for which microchannels were formed. (c) Formation of copper micropillars with a diameter of 190 μm using an electroplating method and subsequent deposition of the inner antenna. (d) Setting the AT-cut quartz resonators. (e) Packaging with the laser-bonding method.

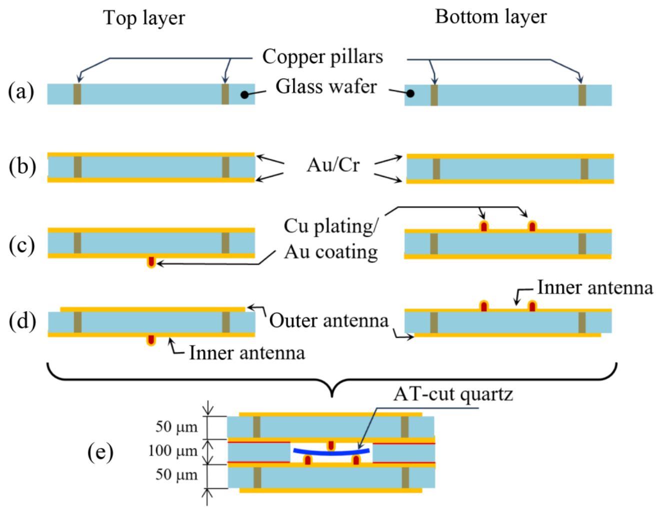

FIG. 9. MEMS process for fabricating 3×3 sensors. (a) Preparation of 4-inch, 50-μm-thick glass wafers with through-glass copper vias with a diameter of 50 μm. (b) Deposition of inner and outer antennas. (c) Formation of copper micropillars with a diameter of 50 μm using the electroplating method and subsequent deposition of a gold thin-film coating. (d) Patterning the outer and inner antennas. (e) Bonding of the top and bottom layers with a 100-μm-thick glass interlayer with microchannels using the gold-tin solder-bonding method.

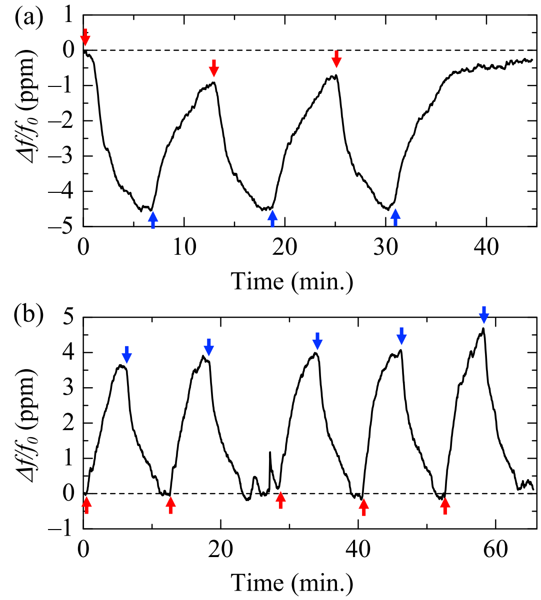

FIG. 11. Changes in the resonant frequency of the 3×3 MEMS-QCM attached to an acrylic-resin cantilever during loading–unloading cycles measured at a distance of 50 m. (a) Tension and (b) compression. A microstage was used to apply the deformation up to 15 μm. The red arrows indicate the application of deformation, while the blue arrows show the onset of the unloading process.

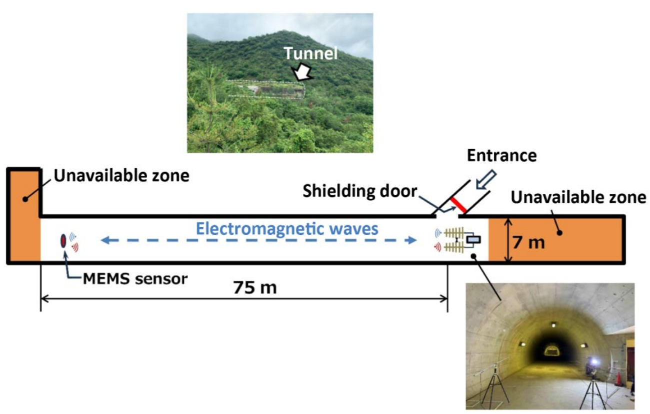

FIG. 10. A 100-m-long tunnel experimental facility buried inside the mountain. The wireless experiments were conducted inside this tunnel with an inner diameter of 7 m, located within the Harima Plant of Daicel Corporation (Tatsuno, Hyogo, Japan).

APPENDIX B: INFLUENCE OF THE IN-PLANE CONTACT STIFFNESS ON THE RESONANT FREQUENCY

Figure 3 shows that the resonant frequency of the quartz resonator increases as its bending deformation progresses. This trend cannot be explained by the change in geometry because the curvature always decreases the resonator's shear-vibration resonant frequency, as demonstrated in Ref. [30]. We therefore introduce the concept of the in-plane contact stiffness at the contact interface between the contact probe and the quartz surface.

Taking the z axis from the top surface to the bottom and considering the partial plane shear waves propagating upward and downward, the shear displacement in the quartz plate takes the following form:

$$u = U_+ \exp\left[\mathrm{j}(\omega t - kz)\right] + U_- \exp\left[\mathrm{j}(\omega t + kz)\right], \qquad \text{(B1)}$$

where U_+ and U_- denote the amplitudes for the downward and upward partial waves, respectively, and ω and k are the angular frequency and wavenumber, respectively. Two boundary conditions are considered. First, the shear stress on the bottom free surface ($z = d$) must be zero, which gives

$$-U_+ e^{-\mathrm{j}kd} + U_- e^{\mathrm{j}kd} = 0, \tag{B2}$$

where d denotes the resonator thickness. Second, the shear force resulting from the shear stress, τ, should be balanced by the force generated by the contact stiffness, K_i, on the upper surface ($z = 0$). To simplify the estimation of this phenomenon, we employ the following weak boundary condition for this:

$$\tau A = \mathrm{j}AGk(-U_+ + U_-) = K_i(U_+ + U_-). \tag{B3}$$

Here, A and G are the surface area and the shear modulus of the quartz resonator, respectively. Equations (B2) and (B3) yield

$$kd\tan(kd) = \frac{K_i}{AG/d} = \frac{K_i}{K_Q}. \tag{B4}$$

Here, $K_Q = AG/d$ indicates the equivalent in-plane spring constant of the quartz plate. Because the contact stiffness K_i is expected to increase as the contact force at the interface increases, the progress of the bending deformation increases the contact stiffness, resulting in the increase in the resonant frequency as shown in Fig. 3(d).

[1] D. H. Sigurdardottir and B. Glisic, On-site validation of fiber-optic methods for structural health monitoring: Streicker bridge, J. Civ. Struct. Health Monit. **5**, 529 (2015).

[2] H. Murayama, D. Wada, and H. Igawa, Structural health monitoring by using fiber-optic distributed strain sensors with high spatial resolution, Photonic Sens. **3**, 355 (2013).

[3] S. Okazaki, H. Nakagawa, S. Asakura, Y. Tomiuchi, N. Tsuji, H. Murayama, and M. Washiya, Sensing characteristics of an optical fiber sensor for hydrogen leak, Sens. Actuators B **93**, 142 (2003).

[4] F. A. A. Nugroho, I. Darmadi, L. Cusinato, A. Susarrey-Arce, H. Schreuders, L. J. Bannenberg, A. B. da Silva Fanta, S. Kadkhodazadeh, J. B. Wagner, T. J. Antosiewicz *et al.*, Metal–polymer hybrid nanomaterials for plasmonic ultrafast hydrogen detection, Nat. Mater. **18**, 489 (2019).

[5] F. Röck, N. Barsan, and U. Weimar, Electronic nose: Current status and future trends, Chem. Rev. **108**, 705 (2008).

[6] R. C. Levy, S. Mattoo, L. A. Munchak, L. A. Remer, A. M. Sayer, F. Patadia, and N. C. Hsu, The collection 6 modis aerosol products over land and ocean, Atmos. Meas. Tech. **6**, 2989 (2013).

[7] W. Gao, S. Emaminejad, H. Y. Y. Nyein, S. Challa, K. Chen, A. Peck, H. M. Fahad, H. Ota, H. Shiraki, D. Kiriya *et al.*, Fully integrated wearable sensor arrays for multiplexed in situ perspiration analysis, Nature (London) **529**, 509 (2016).

[8] S. Emaminejad, W. Gao, E. Wu, Z. A. Davies, H. Y. Y. Nyein, S. Challa, S. P. Ryan, H. M. Fahad, K. Chen, Z. Shahpar *et al.*, Autonomous sweat extraction and analysis applied to cystic fibrosis and glucose monitoring using a fully integrated wearable platform, Proc. Natl. Acad. Sci. U.S.A. **114**, 4625 (2017).

[9] Y. Kim, R. G. Evans, and W. M. Iversen, Remote sensing and control of an irrigation system using a distributed wireless sensor network, IEEE Trans. Instrum. Meas. **57**, 1379 (2008).

[10] G. Mois, S. Folea, and T. Sanislav, Analysis of three IoT-based wireless sensors for environmental monitoring, IEEE Trans. Instrum. Meas. **66**, 2056 (2017).

[11] A. P. Sample, D. J. Yeager, P. S. Powledge, and A. V. Mamishev, Design of an RFID-based battery-free programmable sensing platform, IEEE Trans. Instrum. Meas. **57**, 2608 (2008).

[12] V. Leonov and R. J. M. Vullers, Wearable thermoelectric generators for body-powered devices, J. Electron. Mater. **38**, 1491 (2009).

[13] K. Kaswan, M. Ray, A. Khan, Y.-L. Wang, and Z.-H. Lin, Recent advances in solid-liquid triboelectric nanogenerators for self-powered chemical and biological sensing, npj Biosens. **1**, 13 (2024).

[14] Y. Song, J. Min, Y. Yu, H. Wang, Y. Yang, H. Zhang, and W. Gao, Wireless battery-free wearable sweat sensor powered by human motion, Sci. Adv. **6**, eaay9842 (2020).

[15] W. Huang, Q. Ding, H. Wang, Z. Wu, Y. Luo, W. Shi, L. Yang, Y. Liang, C. Liu, and J. Wu, Design of stretchable and self-powered sensing device for portable and remote trace biomarkers detection, Nat. Commun. **14**, 5221 (2023).

[16] G. Yao, D. Jiang, J. Li, L. Kang, S. Chen, Y. Long, Y. Wang, P. Huang, Y. Lin, W. Cai, and X. Wang, Self-activated electrical stimulation for effective hair regeneration via a wearable omnidirectional pulse generator, ACS Nano **13**, 12345 (2019).

[17] Y. Feng, L. Xie, Q. Chen, and L.-R. Zheng, Low-cost printed chipless RFID humidity sensor tag for intelligent packaging, IEEE Sens. J. **15**, 3201 (2015).

[18] Z. Zhang, Q. Shi, T. He, X. Guo, B. Dong, J. Lee, and C. Lee, Artificial intelligence of toilet (AI-toilet) for an integrated health monitoring system (IHMS) using smart triboelectric pressure sensors and image sensor, Nano Energy **90**, 106517 (2021).

[19] R. S. Andre, R. Schneider, G. R. DeLima, L. Fugikawa-Santos, and D. S. Correa, Wireless sensor for meat freshness assessment based on radio frequency communication, ACS Sens. **9**, 631 (2024).

[20] Y. Kim, J. M. Suh, J. Shin, Y. Liu, H. Yeon, K. Qiao, H. S. Kum, C. Kim, H. E. Lee, C. Choi *et al.*, Chip-less wireless electronic skins by remote epitaxial freestanding compound semiconductors, Science **377**, 859 (2022).

[21] P. Jeltiri, F. Al-Mahmoud, Rémi Boissière, B. Paulmier, T. Makdissy, O. Elmazria, P. Nicolay, and S. Hage-Ali, Wireless strain and temperature monitoring in reinforced concrete using surface acoustic wave sensors, IEEE Sensors Lett. **7**, 1 (2023).

[22] A. Pohl, A review of wireless SAW sensors, IEEE Trans. Ultrason. Ferroelectr. Freq. Control **47**, 317 (2000).

[23] I. Koga, Thickness vibrations of piezoelectric oscillating crystals, Physics **3**, 70 (1932).

[24] F. Kato, H. Ogi, T. Yanagida, S. Nishikawa, M. Hirao, and M. Nishiyama, Resonance acoustic microbalance with naked-embedded quartz (RAMNE-Q) biosensor fabricated by microelectromechanical-system process, Biosens. Bioelectron. **33**, 139 (2012).

[25] L. Zhou, F. Kato, N. Nakamura, Y. Oshikane, A. Nagakubo, and H. Ogi, MEMS hydrogen gas sensor with wireless quartz crystal resonator, Sens. Actuators B **334**, 129651 (2021).

[26] L. Zhou, F. Kato, M. Iijima, T. Nonaka, S. Kuroda, and H. Ogi, Mass-fabrication scheme of highly sensitive wireless electrodeless MEMS QCM biosensor with antennas on inner walls of microchannel, Anal. Chem. **95**, 5507 (2023).

[27] H. Ogi, H. Nagai, Y. Fukunishi, M. Hirao, and M. Nishiyama, 170-MHz electrodeless quartz crystal microbalance biosensor: Capability and limitation of higher frequency measurement, Anal. Chem. **81**, 8068 (2009).

[28] K. Noi, K. Ikenaka, H. Mochizuki, Y. Goto, and H. Ogi, Disaggregation behavior of amyloid β fibrils by anthocyanins studied by total-internal-reflection-fluorescence microscopy coupled with a wireless quartz-crystal microbalance biosensor, Anal. Chem. **93**, 11176 (2021).

[29] K. Noi, A. Iwata, F. Kato, and H. Ogi, Ultrahigh-frequency, wireless MEMS QCM biosensor for direct, label-free detection of biomarkers in a large amount of contaminants, Anal. Chem. **91**, 9398 (2019).

[30] L. Zhou, N. Nakamura, A. Nagakubo, and H. Ogi, Highly sensitive hydrogen detection using curvature change of wireless-electrodeless quartz resonators, Appl. Phys. Lett. **115**, 171901 (2019).

[31] See Supplemental Material at http://link.aps.org/supplemental/10.1103/wv9d-w2fv for seeing the extremely flexible bending behavior of the blank AT-cut quartz crystal resonator measuring $1.8 \times 1.6 \times 0.0131$ mm^3. The quartz plate is supported by 0.2-mm-diameter wires and bent manually using a wooden rod.

[32] H. L. Chao and T. E. Parker, Tensile fracture strength of ST cut quartz, in *Proc. IEEE Freq. Control Symp.* (1983), pp. 116–124.

[33] J. R. Willis, Hertzian contact of anisotropic bodies, J. Mech. Phys. Solids **14**, 163 (1966).

[34] H. Ogi, H. Niho, and M. Hirao, Elastic-stiffness distribution on dual-phase stainless steel studied by resonance ultrasound microscopy, Acta Mater. **54**, 4143 (2006).

[35] H. Ogi, T. Inoue, H. Nagai, and M. Hirao, Quantitative imaging of young's modulus of solids: A contact-mechanics study, Rev. Sci. Instrum. **79**, 053701 (2008).

[36] B. A. Auld, *Acoustic Fields and Waves in Solids* (Wiley, New York, 1973).